Predicting Far-Field Stresses using Finite Element Model Based on Near-Wellbore Machine Learning Estimates for Well 16A(78)-32

Report documenting completion of Milestone 4.2.1 of Utah FORGE Project 2-2439v2: A Multi-Component Approach to Characterizing In-Situ Stress at the U.S. DOE FORGE EGS Site: Laboratory, Modeling and Field Measurement

Guanyi Lu[a], Ayyaz Mustafa[a], and Andrew P. Bunger[a,b,*]

[a] Department of Civil and Environmental Engineering, University of Pittsburgh, Pittsburgh, PA, USA

[b] Department of Chemical and Petroleum Engineering, University of Pittsburgh, Pittsburgh, PA, USA

*Corresponding author: bunger@pitt.edu

Table of Contents

List of Figures

List of Tables

1. Abstract

We report the far-field stress predictions at two locations along the vertical section of well 16A (78)-32 using the physics-based thermo-poro-mechanical model developed in Task 4.1. Three principal stresses in far-field are obtained by solving an inverse problem based on the near-wellbore stress estimates generated by the Machine Learning (ML) model developed in Task 2. We demonstrate the successful implementation of the combined ML and physics-based model to translate the near-field stresses to stresses away from the wellbore/cooling-influenced zone. The thermo-poro-mechanical effect by pre-cooling circulation prior to well logging in an enhanced geothermal system (EGS) well has been taken into consideration in our stress predictions. Our results indicate an isotropic horizontal stress state in the far-field of Well 16A (78)-32.

2. Task and milestone description

The main objective of **Task 4.2** is connecting the near-wellbore data measured at Utah FORGE to the far-field (away from the wellbore) stresses under various thermal conditions using the physics-based model developed in Task 4.1. **Milestone 4.2.1** entails predicting the far-field stresses based on near-wellbore estimates for Well 16A (78)-32.

This report documents the completion of **Milestone 4.2.1** and technical accomplishments as per the Statement of Project Objectives (SOPO) for the project. Stress profiles of the maximum, intermediate, and minimum stress from the wellbore to the far-field along two trajectories with respect to the minimum principal stress direction, as well as far-field stresses at two locations (depths) along the vertical section of the well are provided in this report.

3. Methodology

3.1. Overview

Both field evidence (sonic logging data) and lab TUV (Triaxial Ultrasonic Velocity) measurements indicate the presence of stress-induced anisotropy in FORGE rocks (Bunger et al., 2022; Kelley and Bunger, 2023; Mustafa et al., 2023a). Such anisotropy would lead to varying wave velocities based on the wave type, propagation direction, and polarity. Utilizing this characteristic, the ML model developed in Task 2 is trained and tested with the velocity-to-stress relationship of three waves generated in lab on FORGE rocks – the compressional wave along well axis, and the fast and slow (presumably mutually orthogonal) shear waves in the plane transverse to the wellbore. The resulting predictive model then takes the sonic logging data as the input and estimates all three (the minimum, intermediate, and maximum) in-situ stresses.

It is worth noting that the current ML model does not specify any in-situ conditions such as drilling and pre-cooling activities (i.e., assuming an intact rock formation without any stress perturbation). However, sonic logging is conducted in regions near the well, where strong poro-elastic stress alteration exists due to drilling. Furthermore, extensive circulation of cold fluid along the wellbore interval is often necessary for preventing downhole equipment used in well logging from overheating. These two major factors can work together (or cancel each other depending on the specific in-situ conditions) to significantly alter the near-wellbore stress field and lead to misinterpretation of the in-situ stresses. As a result, the ML predictions can be associated with the local stresses that are induced due to drilling and pre-cooling activities, instead of the actual far-field confining stresses. Hence, it is necessary to characterize the thermo-poro-mechanical effect in near-field and translate the stress fields in the near-field to far-field when interpreting the logging data.

A schematic of a vertical well with the stress/temperature boundary conditions (B.C.s) in 3D is given in Figure 1. The problem is characterized by pre-cooling circulation along an interval of a vertical well with radius r_w in a formation subjected to the minimum, intermediate, and maximum principal stresses ($S_{h\min} < S_{H\max} < S_v$). The pre-cooling circulation is conducted under constant temperature T_w at the borehole, while the reservoir has a uniform initial temperature T_0, and remains constant in far-field throughout the

process. We denote the drop of temperature as $\Delta T = T_w - T_0$. Once pre-cooling stops (at $t = t_c$), the cooling B.C. is removed, and the temperature field during both pre-cooling and the following warmup (at an arbitrary time $t = t_c + t_w$) stages can be solved by the FE model (see and illustration of the temperature evolution on the borehole wall in Figure 2). Additionally, the reservoir is subjected to a uniform virgin pore pressure, p_0. Due to the excavation of the well, a constant mud pressure, p_w, is uniformly distributed along the borehole wall, resulting in a pressure difference, $\Delta p = p_w - p_0$. Consequently, the stress field is determined by (1) three far-field stresses, (2) mud pressure and pore pressure, and (3) the pre-cooling/warmup conditions.

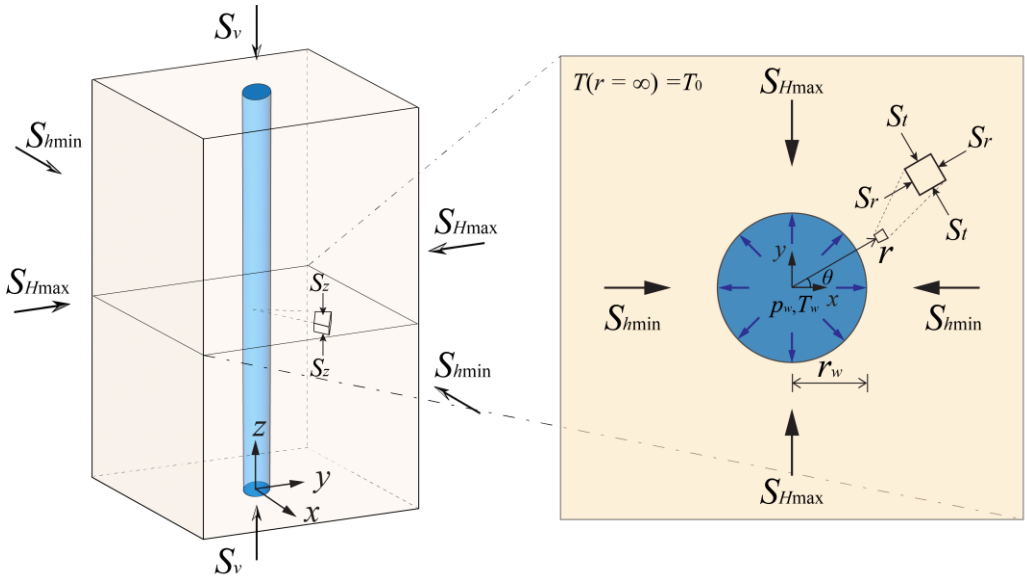

Figure 1: Problem setup of the FE model (right) and planar view of pre-cooling circulation carried out along a vertical borehole (right).

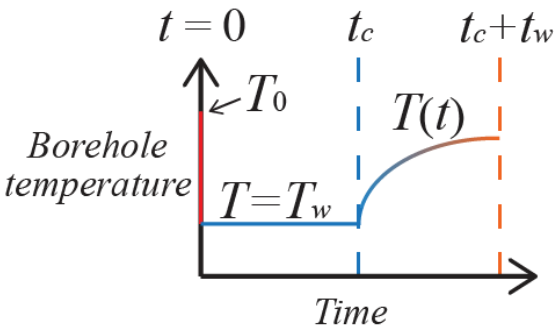

Figure 2: Temperature evolution on borehole wall in the FEM model.

In the near-field, we use a cylindrical coordinate system defined by radius *r*, angle with respect to the intermediate stress direction, θ, and z along the axial direction, to compute the three principal stress components predicted by the ML model - radial stress (S_r), tangential stress (S_t), and the axial stress (S_z). Recall that, the ML model generates the stress predictions based on well logging data of the compressional P-wave velocity, and the fast and slow shear S-wave velocities measured in the nearby rock which are measured under stress induced anisotropy. In this work, we impose that the sonic logging measurements are taken at the location of $r = 4r_w$, which is a reasonable distance based on the configuration of the ThruBit (through-the-bit) logging device utilized at Well 16A (78)-32.

Thanks to its linearity, the overall problem can be decomposed into three components: (I) near-wellbore stress concentration due to the excavation of borehole under mud pressure and far-field stresses, (II) poro-elastic stresses induced by pore pressure diffusion near the well, and (III) thermally induced stresses near the borehole due to heat conduction in pre-cooling and warmup. In our analysis, the poro-elastic stresses in part II can be computed based on existing semi-analytical solutions (Cheng, 2016; Gao

et al., 2016), and the thermally induced stresses in part III are obtained by FEM modeling. We then use linear superposition to compute the total thermo-poro-elastic stresses, written as:

$$S = S^{\mathrm{I}} + S^{\mathrm{II}} + S^{\mathrm{III}} \tag{1}$$

Note that this linear superposition is valid under one important assumption: the thermally induced pore pressure in part III (not the pore pressure diffusion in part II) is negligible compared to all stress components in Eq. (1).

3.2. Analytical solutions

Both drilling induced stress concentration (S^{I}) under the mud pressure (p_w) and three far-field stresses ($S_{h\min}$, $S_{H\max}$, and S_v), and the poro-elastic stresses (S^{II}) due to pressure diffusion can be solved using semi-analytical solutions (e.g., Cheng, 2016; Gao et al., 2016). For S^{I}, the three stress components can be computed by:

$$S_t^{\mathrm{I}} = -\left(1+\frac{r_w^2}{r^2}\right)P_0 - \left(1+3\frac{r_w^4}{r^4}\right)S_0\cos 2\theta + \frac{r_w^2}{r^2}p_w \tag{2a}$$

$$S_r^{\mathrm{I}} = -\left(1-\frac{r_w^2}{r^2}\right)P_0 + \left(1-4\frac{r_w^2}{r^2}+3\frac{r_w^4}{r^4}\right)S_0\cos 2\theta - \frac{r_w^2}{r^2}p_w \tag{2b}$$

$$S_z^{\mathrm{I}} = -S_v - 4\nu\frac{r_w^2}{r^2}S_0\cos 2\theta \tag{2c}$$

in which $P_0 = \frac{S_{H\max}+S_{h\min}}{2}$, $S_0 = \frac{S_{H\max}-S_{h\min}}{2}$, Generally, ThruBit logging is conducted after the well has been drilled. The delay can be a few hours. Hence, we use the transient solutions for computing the poro-elastic stresses (part II). Given the constant pressure boundary conditions ($p = p_w$ at borehole wall and $p = p_0$ in the far-field), the stresses and pore pressure are obtained in Laplace transform domain, denoted by $\tilde{S}^{\mathrm{II}}$ and $\tilde{p}^{\mathrm{II}}$. Their values are given by (Cheng, 2016)

$$\frac{s\tilde{S}_t^{\mathrm{II}}}{p_w - p_0} = -2\eta\left[\frac{1}{r^*}\frac{\mathrm{K}_1\left(r^*\sqrt{s^*}\right)}{\sqrt{s^*}\mathrm{K}_0\left(\sqrt{s^*}\right)} - \frac{1}{r^{*2}}\frac{\mathrm{K}_1\left(\sqrt{s^*}\right)}{\sqrt{s^*}\mathrm{K}_0\left(\sqrt{s^*}\right)} + \frac{\mathrm{K}_0\left(r^*\sqrt{s^*}\right)}{\mathrm{K}_0\left(\sqrt{s^*}\right)}\right] \tag{3a}$$

$$\frac{s\tilde{S}_r^{\mathrm{II}}}{p_w - p_0} = 2\eta\left[\frac{1}{r^*}\frac{\mathrm{K}_1\left(r^*\sqrt{s^*}\right)}{\sqrt{s^*}\mathrm{K}_0\left(\sqrt{s^*}\right)} - \frac{1}{r^{*2}}\frac{\mathrm{K}_1\left(\sqrt{s^*}\right)}{\sqrt{s^*}\mathrm{K}_0\left(\sqrt{s^*}\right)}\right] \tag{3b}$$

$$\frac{s\tilde{p}_\Delta^{\mathrm{II}}}{p_w - p_0} = \frac{\mathrm{K}_0\left(r^*\sqrt{s^*}\right)}{\mathrm{K}_0\left(\sqrt{s^*}\right)} \tag{3c}$$

where $r^* = \frac{r}{r_w}$, $s^* = \frac{r_w^2 s}{c}$ with s denoting the Laplace transform parameter, and η is the poro-elastic stress coefficient. A numerical inversion method (Stehfest, 1970) is then applied to evaluate the stress components in Eqs. (3abc). The overall pressure is then computed by $p^{\mathrm{II}} = p_\Delta^{\mathrm{II}} + p_0$. In addition, the axial stress under the plane-strain condition is expressed as

$$S_z^{\mathrm{II}} = \nu\left(S_t^{\mathrm{II}} + S_r^{\mathrm{II}}\right) - \alpha(1-2\nu)\left(p^{\mathrm{II}} - p_0\right) \tag{3d}$$

in which α is the Biot effective stress coefficient $\left(\alpha = \frac{2\eta(1-\nu)}{1-2\nu}\right)$.

3.3. FEM model

Next, the FEM model developed in Task 4.1 has been upgraded (both in geometry and mesh) to improve its accuracy in computing the radial heat conduction and its induced thermal stresses, S_t^{III}, S_r^{III}, and S_r^{III}. Two subproblems are solved sequentially:

Subproblem 1: Pre-cooling and warmup lead to temperature change near the borehole. To model the heat transfer from the borehole to the reservoir, The cold fluid circulation begins at $t = 0$ and ends at t_c. The warmup duration is characterized by t_w.

Subproblem 2: After obtaining the temperature field associated with pre-cooling/warmup, we then impose this temperature distribution as a pre-defined field variable in a thermo-mechanical problem setup. The resulting thermo-elastic stress fields caused by heat transfer in reservoir is then computed.

The problem of pre-cooling/warmup induced stresses surrounding a circular wellbore is solved using a one-way coupled setup (heat transfer causes mechanical deformation but the deformation in rocks does not affect the temperature distribution). The entire problem is modelled in a 2.5-m radius circular domain (Figure 3). Mesh in areas near the borehole is refined to capture the expected sharp stress/strain gradient. A total of 19,521 nodes and 6400 elements are generated. For the heat transfer subproblem 1, the heat transfer is modelled with DC2D8 elements (8-node quadratic heat transfer quadrilateral element). For the thermo-mechanical subproblem 2, we use CPE8 (8-node biquadratic plane strain quadrilateral element).

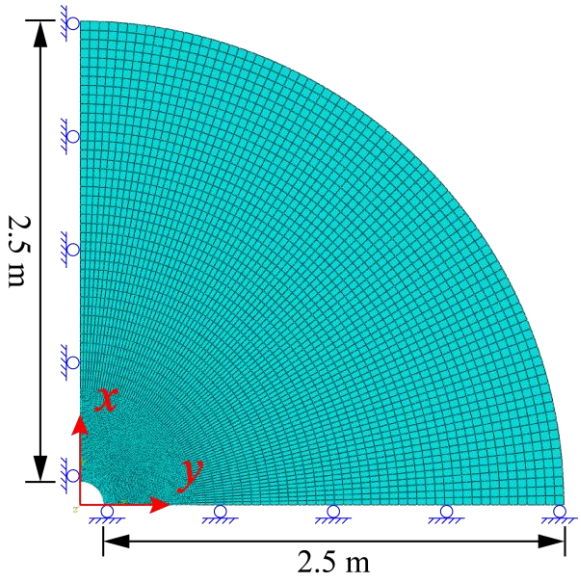

Figure 3: Mesh and boundary conditions of both subproblems generated in ABAQUS.

3.4. Input parameters

Realistic values of thermo-poro-mechanical properties of granitic rocks were used in our stress analaysis (Table 1).

Young's modulus (E)	37.5 GPa
Poisson's ratio (ν)	0.25
Density (ρ)	2710 kg/m^3
Thermal conductivity (k_T)	2.5 $\mathrm{W/(m \cdot K)}$
Volumetric thermal expansion coefficient (β_d)	8×10^{-6} K^{-1}
Thermo-elastic stress coefficient (η_d)	2×10^5 $\mathrm{N/(m^2 \cdot K)}$
Poro-elastic stress coefficient (η)	0.08

Biot effective stress coefficient (α)	0.24
Reservoir temperature (T_0)	150 ˚C
Pre-cooling temperature (T_w)	110 ˚C
Pre-cooling duration (t_c)	10 hours
Warmup duration (t_w)	4 hours
Wellbore pressure (p_w) (mud weight 9.5 ppg)	Location 1: 18.7 MPa Location 2: 19.9 MPa
Virgin pore pressure (p_0)	Location 1: 16.4 MPa Location 2: 17.5 MPa
ML predicted maximum far-field stress (S_v)	Location 1: 41 MPa Location 2: 43.1 MPa
ML predicted intermediate far-field stress ($S_{H\max}$)	Location 1: 31 MPa Location 2: 34.2 MPa
ML predicted minimum far-field stress (S_{hmin})	Location 1: 27.1 MPa Location 2: 29 MPa
Wellbore radius (r_w)	0.12 m

Table 1: Input parameters.

4. Result

We first note that the stress values predicted by the ML model are purely based on sonic logging data assuming they are collected in an intact rock formation without any near-field stress disturbance. To study the impact of near-wellbore thermo-poro-elastic stress alteration, we will the ML model predictions as the far-field stresses (Table 1) and transform them to near-field regions where the actual logging data is collected. Then, we will invert the problem by imposing these values as the near-field thermo-poro-elastic stresses and compute their corresponding far-field stresses.

4.1. Stresses along two trajectories

The ML predictions obtained in Task 2 is shown in Figure 4 (see more details in Milestone reports of Task 2). The two locations where core samples were collected, and lab triaxial ultrasonic wave velocity measurements were conduct on are at 5474 ft and 5850 ft, both along the vertical section of the well. Their respective stress predictions are:

Location 1 - $S_1(S_v)$ = 41.04 MPa, $S_2(S_{H\max})$ = 31 MPa, $S_3(S_{h\min})$ = 27.07 MPa.

Location 2 - $S_1(S_v)$ = 43.12 MPa, $S_2(S_{H\max})$ = 34.15 MPa, $S_3(S_{h\min})$ = 28.98 MPa.

Since the conclusions drawn from the stress analyses at both locations are identical, we will focus on location 1 (5474 ft) as an illustration of the thermo-poro-mechanical effect.

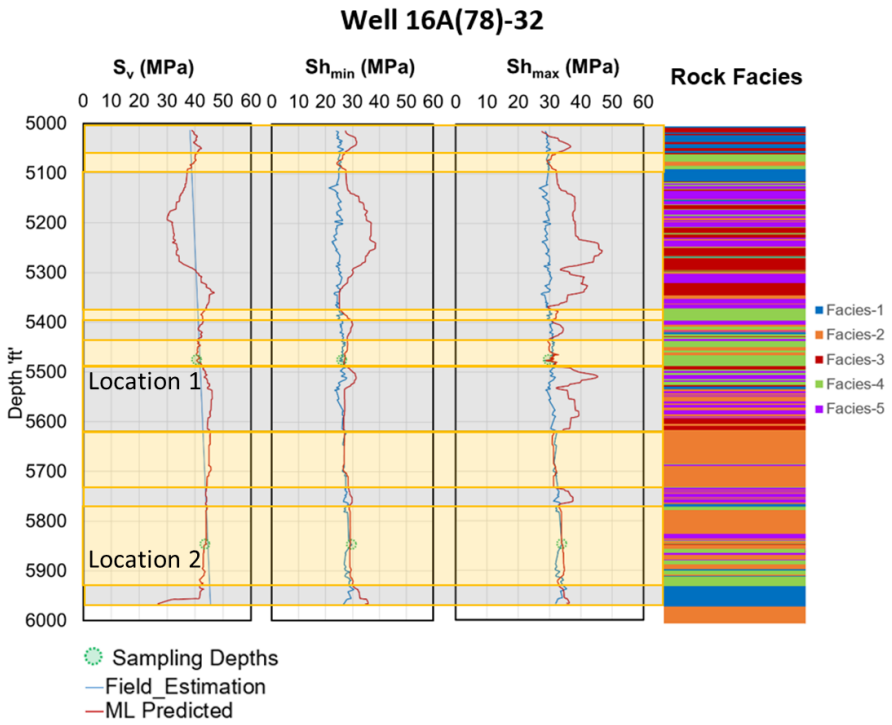

Figure 4: Estimated in-situ stresses in the well 16A(78)-32 and corresponding rock facies obtained in ML model (Mustafa et al., 2023a,b).

While both poro-elastic (II) and thermo-elastic (III) stresses are axisymmetric due to the nature of radial diffusion, and they remain constant with varying angle θ (Figure 1), S^{I} values (drilling induced stress concentration) change with $\theta \in \left[0, \frac{\pi}{2}\right]$. Figure 4 depicts the variation of S^{I} with θ at $r = 4r_w$, where the wave speed measurements are collected. The two stresses, S_t^{I} and S_r^{I}, are shown to be monotonically increasing/decreasing with θ, while S_z^{I} remains somewhat constant. Based on these observations, we will use the two extreme values of stresses at $\theta = 0$ and $\theta = \frac{\pi}{2}$ to determine the least and largest near-field stress values under the influences of stress concentration, the axi-symmetric heat transfer and pore pressure diffusion, namely, the three principal stresses can only exist among the following stresses: $S_r(\theta = 0)$, $S_t(\theta = 0)$, $S_z(\theta = 0)$, $S_r\left(\theta = \frac{\pi}{2}\right)$, $S_t\left(\theta = \frac{\pi}{2}\right)$, $S_z\left(\theta = \frac{\pi}{2}\right)$.

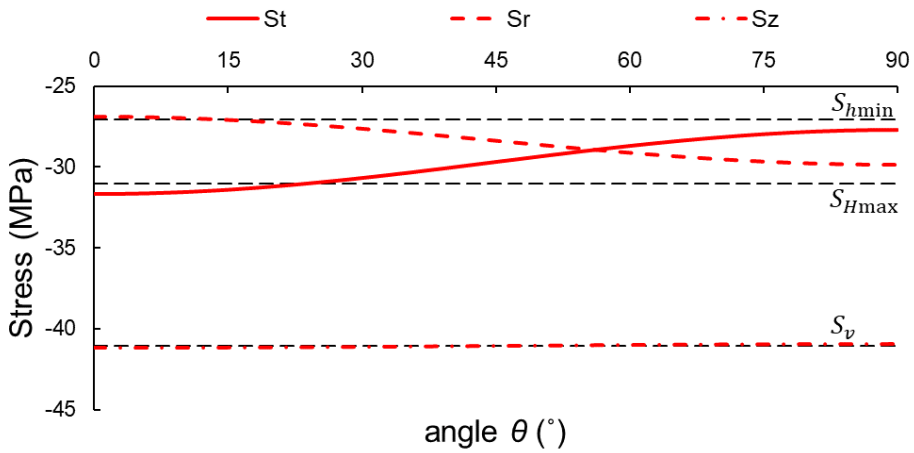

Figure 5: Variation of S_t^{I}, S_r^{I}, and S_z^{I} with θ at $r = 4r_w$.

The distribution of all three (total) stress components along two trajectories, $\theta = 0$ and $\theta = \frac{\pi}{2}$, are depicted in Figure 6. Three pre-cooling scenarios are considered: (1) isothermal field, with $S^{\mathrm{III}} = 0$; (2) 10-hour simultaneous pre-cooling circulation and pore pressure diffusion with pressure and temperature

boundary conditions of t_c=10 hours, T_w=110 ˚C, T_0=150 ˚C, p_w=18.7 MPa (location 1) and 19.9 MPa (location 2), and p_0=16.4 MPa (location 1) and 17.5 MPa (location 2); (3) followed by 4 hours of warmup (t_w=4 hours). Wellbore pressure is held constant throughout both pre-cooling and warmup stages. All input parameters are given in Table 1. Thus, the effect of pore pressure diffusion is shown by the isothermal case, and the thermal effect during both pre-cooling and warmup stages are illustrated by cases (1) and (2).

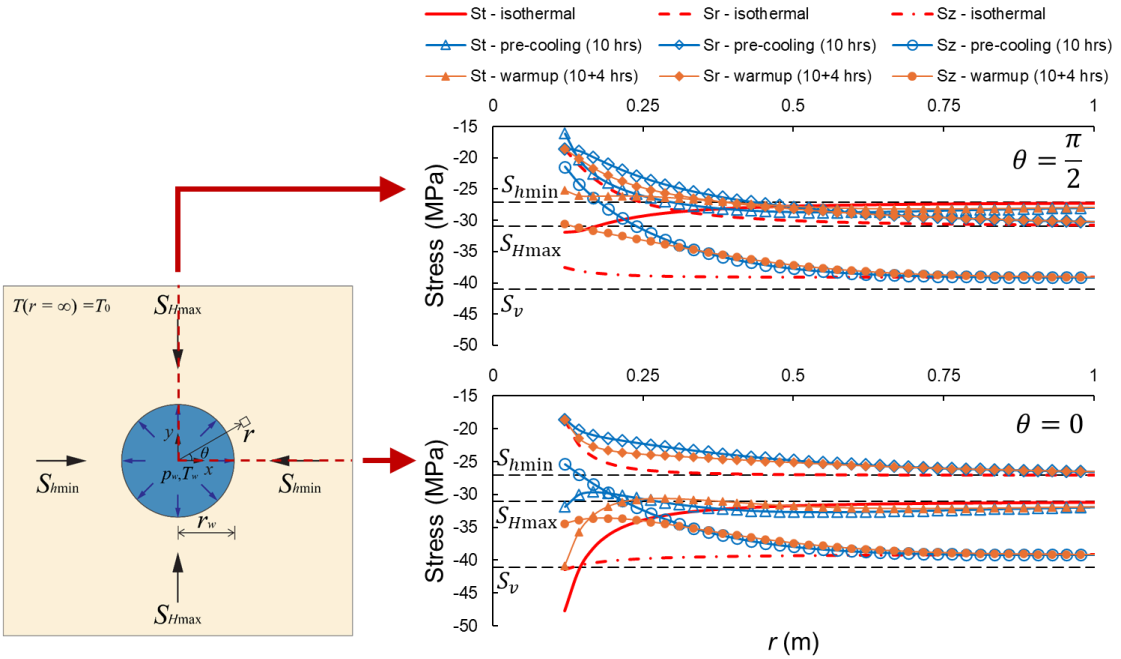

Figure 6: Distribution of stresses along two trajectories ($\theta = 0$ and $\theta = \frac{\pi}{2}$) in three scenarios: (1) in an isothermal field with zero thermally induced stresses (S^{III}), (2) immediately after 10-hour borehole pre-cooling circulation, and (3) another 4-hour waiting period. For comparison, the three far-field stresses are also plotted.

Notable near-field alteration (difference between the three near-field principal stresses and their corresponding far-field stresses) is observed in all three stress components, with the largest stress discrepancy at the borehole wall ($r = r_w$). The perturbation diminishes with increasing distance from the wellbore. Interestingly, the alteration is seen to be less in S_r than in S_t and S_z.

4.2. Determining near-field stress components for ML model

Next, we examine the stresses at $r = 4r_w$ (where the sonic logging data is supposedly collected) in both 0 and $\frac{\pi}{2}$ orientations in Table 2. In both pre-cooling and subsequent warmup scenarios, the minimum, intermediate, and maximum principal stresses are found at $\theta = 0$, whereas a somewhat uniform horizontal stress state (S_r and S_t) is observed at $\theta = \frac{\pi}{2}$. It is thus sensible to associate the fast and slow shear waves' polarities with the two extreme stress values at $\theta = 0$. The three near-field principal stress components that correspond to the velocity-to-stress ML model predictions in near-field are:

$$\theta = 0, r = 4r_w\text{: } S_r(S_{h\min}) < S_t(S_{H\max}) < S_z(S_v)$$

	S_r (MPa)	S_t (MPa)	S_z (MPa)
10-hr pre-cooling ($\theta = 0$)	**24.65**	**32.63**	**37.69**
10-hr pre-cooling ($\theta = \frac{\pi}{2}$)	27.63	28.65	37.44
4-hr warmup ($\theta = 0$)	**25.06**	**31.65**	**37.13**
4-hr warmup ($\theta = \frac{\pi}{2}$)	28.05	27.68	36.89

Table 2: Total (compressive) stresses in both pre-cooling/warmup scenarios at $r = 4r_w$ for $\theta = 0$ and $\theta = \frac{\pi}{2}$.

The far-field stresses and total thermo-poro-elastic stresses are compared in Figure 7. Overall, S_1 (S_v) and S_3 ($S_{h\min}$) drop as they are transformed to S_z and S_r in both pre-cooling and warmup cases, while S_2 ($S_{H\max}$) increases as it is converted to S_t in near-field. If these ML predictions are directly used as the far-field stresses (despite that they are collected under near-field stress state), we conclude that the ML model would underestimate S_v and $S_{h\min}$, and slightly overestimate $S_{H\max}$.

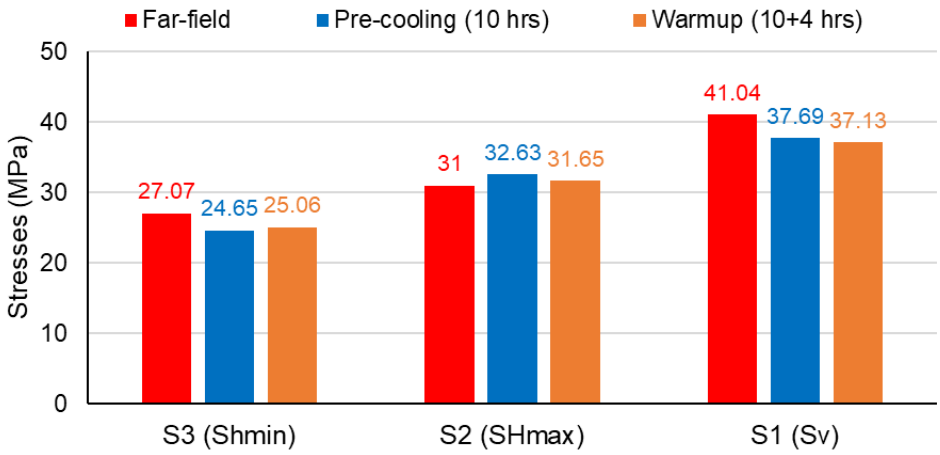

Figure 7: Far-field stresses and total stresses computed at location $\boldsymbol{\theta = 0, r = 4r_w}$.

4.3. Translating near-field ML predictions to far-field stresses

By imposing these ML predictions as the near-field stresses (measured after a 4-hr warmup period following a 10-hour pre-cooling circulation) and solving the inverse problem to find the corresponding far-field stresses, we can obtain their values at both locations:

Location 1

S_r=27 MPa, S_t=30.2 MPa, S_z=41.1 MPa ⇔ $\boldsymbol{S_{h\min}}$**=29.5 MPa,** $\boldsymbol{S_{H\max}}$**=29.5 MPa,** $\boldsymbol{S_v}$ **= 45.1 MPa**

Location 2

S_r=29 MPa, S_t=34.2 MPa, S_z=43.1 MPa ⇔ $\boldsymbol{S_{h\min}}$**=31.4 MPa,** $\boldsymbol{S_{H\max}}$**=33.4 MPa,** $\boldsymbol{S_v}$ **= 47.2 MPa**

The two horizontal far-field stresses at location 1 are more isotropic than the ML predictions – $S_{h\min} = S_{h\max}$ at location 1, and only 2 MPa difference between $S_{h\min}$ and $S_{h\max}$ is observed at location 2. This is likely because wellbore stress concentration generally magnifies the differential stress in the near-field. The vertical stress, S_v, on the other hand, is larger than S_z at both locations.

5. Conclusions

Our overall goal is to develop a reliable velocity-to-stress model (combining both ML and physics-based methods) for predicting the in-situ stresses using field sonic logging data in EGS wells. Because (1) the ML model developed in Task 2 utilizes the wave velocity-stress correlations determined in lab tests, and (2) the wave velocities are measured by sonic logging conducted near the borehole under in-situ conditions (i.e., collected in adjacent rocks where significant thermo-poro-elastic stress alterations are present), the near-field stress predictions do not necessarily correspond to the stresses along directions of the three principal stresses in far-field (i.e., the minimum, intermediate, and maximum in-situ stresses). It is necessary to establish the link between stresses in the near-field and far-field using a physics based thermo-poro-mechanical model.

In this report, we have applied the thermo-poro-mechanical model for estimating the in-situ stresses based on near-field sonic logging data at an EGS well. Stress predictions are carried out using both field and experimental data obtained at Well 16A(78)-32. Future work will consist of (1) integrating the thermo-

poro-mechanical model into the ML model for in-situ stress estimation, and (2) applying the combined ML and physics-based model to estimate far-field stresses at Well 16B(78)-32.

6. References

Bunger, A., Higgins, J., Huang, Y., & Kelley, M. (2022). Utah FORGE Project 2439: A Multi-Component Approach to Characterizing In-Situ Stress. United States. https://dx.doi.org/10.15121/1923003

Cheng, A. H. D. (2016) Poroelasticity. Springer.

Gao, Y., Liu, Z., Zhuang, Z., Hwang, K. C., Wang, Y., Yang, L., & Yang, H. (2016). Cylindrical borehole failure in a poroelastic medium. Journal of Applied Mechanics, 83(6), 061005.

Mustafa, A., Kelley, M., & Bunger, A. (2023a). Training Machine Learning Algorithms to Laboratory Triaxial Ultrasonic Velocity Data for Utah FORGE Well 16A(78)-32. United States. https://gdr.openei.org/submissions/1519

Mustafa, A., Kelley, M., Lu, G., & Bunger, A. (2023b). An Integrated Machine Learning Workflow to Estimate In-situ Stresses Based on Downhole Sonic Logs and Laboratory Triaxial Ultrasonic Velocity Data. Submitted to Journal of Geophysical Research - Machine Learning and Computation. (Under review)

Kelley, M., Bunger, A. (2023). Utah FORGE 2-2439: A Multi-Component Approach to Characterizing In-Situ Stress: Laboratory, Modeling and Field Measurement - Workshop Presentation. United States. https://dx.doi.org/10.15121/2001502

Stehfest, H. (1970). Numerical inversion of Laplace transforms. Communications of the ACM, 13:47–49.